

Source Characteristics, Site Effects, and Path Attenuation from Spectral Analysis of Strong-Motion Recordings in the 2016 Kaikōura Earthquake Sequence

by Yefei Ren, Ying Zhou, Hongwei Wang, and Ruizhi Wen

Abstract This study used the spectral inversion technique to investigate the source characteristics, site effects, and path attenuation of *S*-wave Fourier amplitude spectra recorded in the M_w 7.8 Kaikōura, New Zealand, earthquake sequence. For this purpose, we assembled a dataset comprising 2445 strong-motion recordings, obtained at 126 GeoNet stations, of 148 earthquakes in this sequence with local magnitudes of 4.02–6.16. The seismic moment, corner frequency, and stress drop for each earthquake were estimated based on the inverted source spectra. Investigation of the characteristics of these source parameters revealed the following. (1) The seismic moment is inversely proportional to the cube of the corner frequency, implying that the Kaikōura earthquake sequence within the investigated magnitude range followed self-similarity. (2) The stress drop varied predominantly from 0.2 to 6.0 MPa with a logarithmic mean of 1.25 MPa, and it did not show any evidence of dependence on magnitude size and focal depth. Investigation of the features of the site-response functions of the 126 strong-motion stations inverted in this study revealed the following. (1) Linear relationships between the site amplification and site characteristic parameters V_{S30} and T_{site} at each frequency point of 0.5–3.0 Hz were regressed with correlation coefficients of 0.5–0.8, indicating that site amplification correlates moderately with both parameters. (2) Site amplification in the Wellington region exhibited strong correlation with the geological and geotechnical characterization, for example, the depth of the soil deposit. (3) Strong site amplification appeared considerable in the Christchurch Central Business District. The inverted *S*-wave quality factor was regressed to $130.87f^{1.07}$ at frequencies of 0.5–20.0 Hz. No significant regional dependence of anelastic attenuation was identified in the study region.

Electronic Supplement: Figure showing site-response functions of 126 strong-motion stations inverted by this study, and table of the inverted source parameters for 148 aftershock events in the 2016 Kaikōura earthquake sequence, estimated by the spectral inversion technique.

Introduction

The 2016 M_w 7.8 Kaikōura earthquake was the largest earthquake recorded in New Zealand since the 1855 M_w 8.2 Wairarapa earthquake (epicenter shown in Fig. 1), and it has aroused great concern among earthquake scientists and engineers worldwide. The Kaikōura earthquake initiated in the Waiau plains of North Canterbury (South Island, New Zealand), where the extremely complex tectonic regime is characterized by the transition from the southern Hikurangi subduction zone to the oblique continental convergence dominated by the strike-slip Alpine fault (Kaiser, Balfour, *et al.*,

2017). One remarkable feature of the Kaikōura earthquake was its exceptional rupture complexity (Hamling *et al.*, 2017). Geodetic and field observations revealed surface ruptures on at least 12 major faults. The rupture of such a large number of faults in a single earthquake event requires the definition of rupture scenarios in seismic hazard models to be reconsidered. Investigating the source characteristics (e.g., scaling relations of source parameters) of this earthquake sequence constitutes one of the vital procedures necessary for re-evaluating seismic hazard near seismogenic faults.

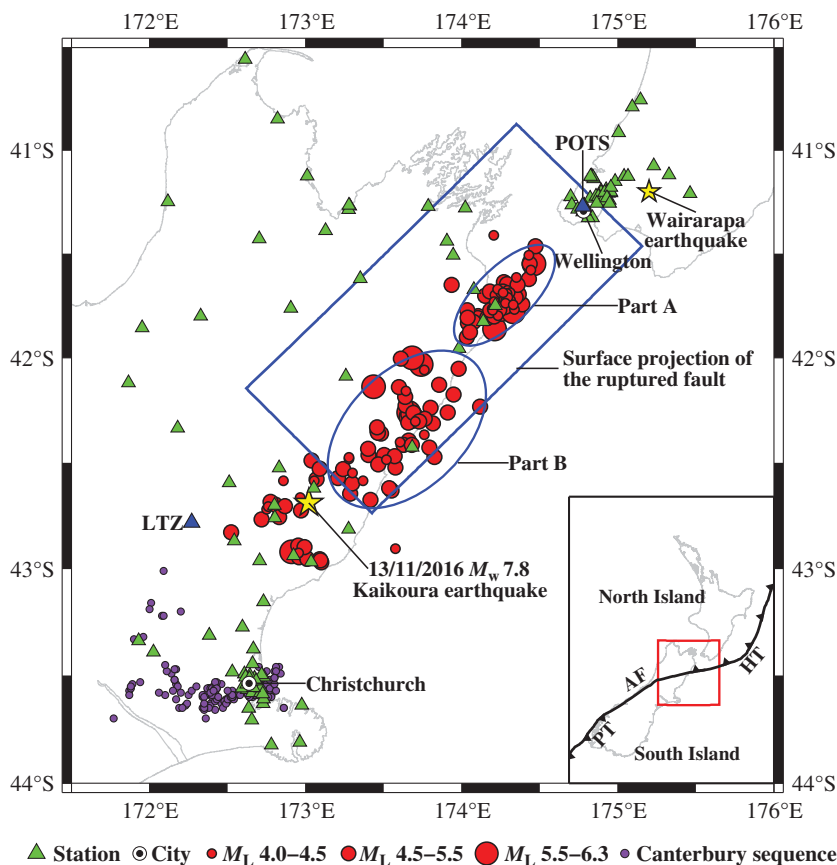


Figure 1. Locations of earthquakes (circles) and strong-motion stations (triangles) considered in this study. Two stars indicate the epicenters of the 2016 M_w 7.8 Kaikōura earthquake and the 1855 Wairarapa earthquake, respectively. Blue triangles represent two reference stations (LTZ and POTS) used in the inversion. The blue box indicates the surface projection of the second segmentation of the fault rupture plane provided by the U.S. Geological Survey (USGS; see [Data and Resources](#)). Earthquakes enclosed in the two ellipses were divided into part A and part B to analyze the lateral variations of stress drop, as shown in Figure 9. Purple circles indicate the epicenters of the 2010–2011 Canterbury earthquake sequences analyzed in the study of [Oth and Kaiser \(2014\)](#). (Inset) The red rectangle indicates the location of the study region in New Zealand. AF, Alpine fault; HT, Hikurangi trench; PT, Puysegur trench.

The Kaikōura earthquake caused extremely large ground motions, such as the peak ground acceleration (PGA) of 2.7g recorded at station WTMC and 1.2g recorded at station KEKS ([Bradley, Razafindrakoto, and Polak, 2017](#)). The severe shaking of the ground generated notable surface responses such as extreme rupture displacement of up to 9–11 m horizontally and 6–8 m vertically ([Litchfield et al., 2016](#); [Stirling et al., 2017](#)), tens of thousands of landslides ([Dellow et al., 2017](#)), and widespread liquefaction ([Cubrinovski et al., 2017](#)). Consequently, the earthquake caused severe damage to many human-made structures such as concrete buildings ([Henry et al., 2017](#)) and lifeline facilities (e.g., [Hughes et al., 2017](#); [Palermo et al., 2017](#)). The city of Wellington sustained considerable societal impact, even though it was approximately 60 km from the causative earthquake rupture. One of the reasons for this could have been site-effect amplification of long-period ground motions ($T = 1\text{--}2$ s), which at some locations

exceeded the current 500-yr return period design level of ground motion ([Bradley, Wotherspoon, and Kaiser, 2017](#); [Bradley et al., 2018](#)). The period range of 1–2 s corresponds approximately to the resonant periods of mid-rise structures (8–15 stories), which were the focus of much of the damage ([Henry et al., 2017](#); [Kaiser, Balfour, et al., 2017](#)). These observations emphasize the importance of appropriate consideration of site effects in design codes. Further detailed investigation of the site effects associated with this earthquake sequence is required because previous studies focused only on a dozen strong-motion stations (e.g., [Bradley, Wotherspoon, and Kaiser, 2017](#); [Bradley et al., 2018](#)).

The goal of this study was therefore to conduct comprehensive analyses of both the source spectral characteristics of the Kaikōura earthquake sequence and the site effects revealed at many strong-motion stations based on the rich database of strong-motion recordings provided by GeoNet. Similar studies were performed by [Kaiser et al. \(2013, 2016\)](#) and [Oth and Kaiser \(2014\)](#) to simultaneously analyze the source characteristics, path attenuation, and site effects in the 2010–2011 Canterbury earthquake sequence using the spectral inversion method. This technique was also used in this study to separate the source, path, and site contributions to the ground-motion spectra recorded in the Kaikōura earthquake sequence. The source parameters were estimated from the inverted source spectra then to study the source-scaling relations of this earthquake sequence. The site effects considered in this study were site amplification and predominant frequency within this region, especially near Wellington and Christchurch. Finally, the path effect, represented by the quality factor (Q), was analyzed in relation to the regional dependence.

Dataset

GeoNet, established in 2001, integrates multiple hazard monitoring networks in New Zealand, comprising hundreds of seismic and strong-motion stations, Global Positioning System monuments, tsunami gauges, and volcano and landslide surveillance instruments ([Petersen et al., 2011](#)). GeoNet officially released 12,313 strong-motion recordings collected at 264 stations in 367 earthquakes with local magnitudes (M_L) of 4.00–6.26, which occurred as part of the Kaikōura earthquake sequence from 13 November 2016 to 1 March 2017. Most of the earthquakes occurred in the shallow crust

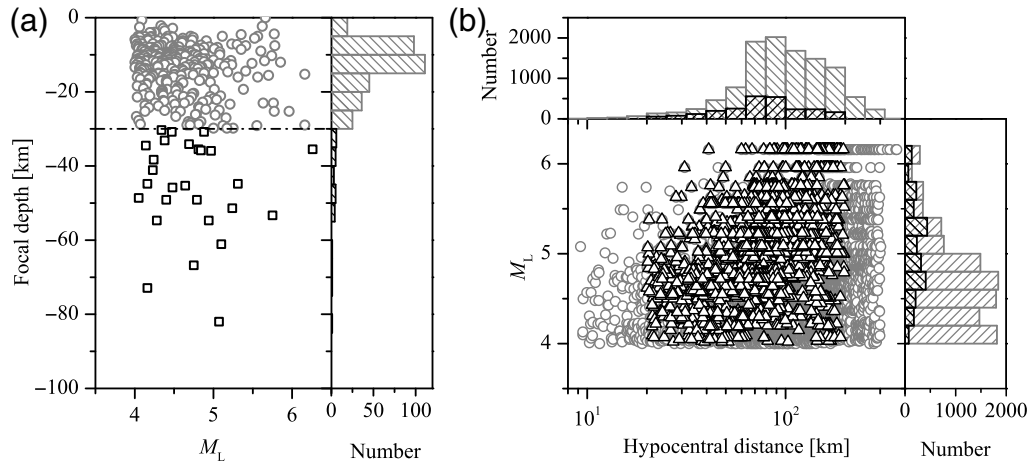


Figure 2. (a) Distribution of local magnitude (M_L) versus focal depth and histogram of focal depths for all events recorded by GeoNet in the Kaikōura earthquake sequence from 13 November 2016 to 1 March 2017. Squares and circles indicate earthquakes with focal depths deeper and shallower than 30 km, respectively. (b) Distribution of M_L versus hypocentral distance and histogram of hypocentral distance and magnitude. Triangles and circles indicate recordings included in the dataset and all recordings with $d \leq 30$ km provided by GeoNet, respectively.

with focal depths (d) ≤ 30 km, and most recordings were obtained at stations with hypocentral distances (R) of 20–300 km from these shallow events, as shown in Figure 2a,b.

This study used a dataset constructed according to the following criteria: (1) $d \leq 30$ km, (2) $20 \leq R \leq 200$ km, (3) $2 \leq \text{PGA} \leq 100$ cm/s², and (4) each selected earthquake should be recorded by at least four stations, each of which should collect at least four recordings that match criteria 1–3. Criteria 1 and 2 ensured most data were included in the required ranges. Recordings for $R \leq 200$ km were considered to reduce the contaminations from the coda wave to the extracted S wave. The occurrence of widespread liquefaction reported by [Cubrinovski et al. \(2017\)](#) and [Stringer et al. \(2017\)](#) indicates the possible existence of nonlinear soil behavior in the Kaikōura earthquake. Recordings with $\text{PGA} < 100$ cm/s² were used to avoid the existence of nonlinear soil behavior as much as possible. The applied spectral inversion scheme is based on the assumption of linear soil response. The occurrence of nonlinear soil behavior will bias the inverted source spectra.

The empirical criterion of $\text{PGA} > 2.0$ cm/s² was used to substantially ensure that the S -wave signal is strong enough to balance the contamination of the ambient noise. Generally, the signal-to-noise ratio (SNR) is necessary to consider in the process of data processing to ensure the data quality. However, most recordings from the Kaikōura earthquake sequence were collected in the aftershocks occurring in the first 3 days (13–15 November) after the mainshock. These recordings generally consist of more than one wave packet, inferred as a result of multiple aftershocks occurring continuously in an extremely short intervals (\sim dozens of seconds). It is rather difficult to extract the pre-event noise of such recordings so that the SNR calculation could be achieved. Such criterion was also used in the spectral analyses of the great Wenchuan earthquake sequence ([Ren et al., 2013](#); [Wang et al., 2018](#)).

As for the Kaikōura earthquake sequence, most recordings in the Wenchuan earthquake sequence include multiple wave packets.

Overall, 2445 strong-motion recordings from 148 earthquakes for M_L 4.02–6.16 recorded at 126 strong-motion stations were assembled in the dataset that was used for the inversion, as shown in Figure 2b. A relatively small magnitude range was covered in this study. The recordings used in the inversion account for only a small proportion of the total of this earthquake sequence, of which about 50% were obtained from aftershocks with $M_L > 5.0$. The geographical locations of the stations and earthquakes considered in this dataset are marked in Figure 1. Note the dense clustering of stations near Wellington and Christchurch that allowed us to investigate the site effects and regional dependence of Q by focusing on both regions.

All recordings included in the dataset were processed using a Butterworth filter with various bandwidths: 0.25–25.0 Hz for recordings collected in earthquakes with $M_L < 4.5$, 0.2–25.0 Hz for $4.5 \leq M_L < 5.5$, and 0.1–25.0 Hz for $M_L \geq 5.5$. The S -wave window was automatically extracted according to the Husid function proposed by [Husid \(1967\)](#) and the cumulative root mean square (rms) function of [McCann and Shah \(1979\)](#) in this study. The arrival of the S wave was identified as the abruptly increased point in the Husid plot, and the end of the S wave was the point in which the cumulative rms function starts to decrease along the time axis. A typical example illustrating this technique is shown in Figure 3a. However, for the recordings including multiple wave packets, the above-mentioned method is invalid, and we extracted the S -wave window from visual inspection (Fig. 3b).

The minimum S -wave window length was related to the magnitude size, 10 s for $M_L \geq 5.5$, 5 s for $4.5 \leq M_L < 5.5$, and 4 s for $M_L < 4.5$ to ensure minimum spectral resolutions

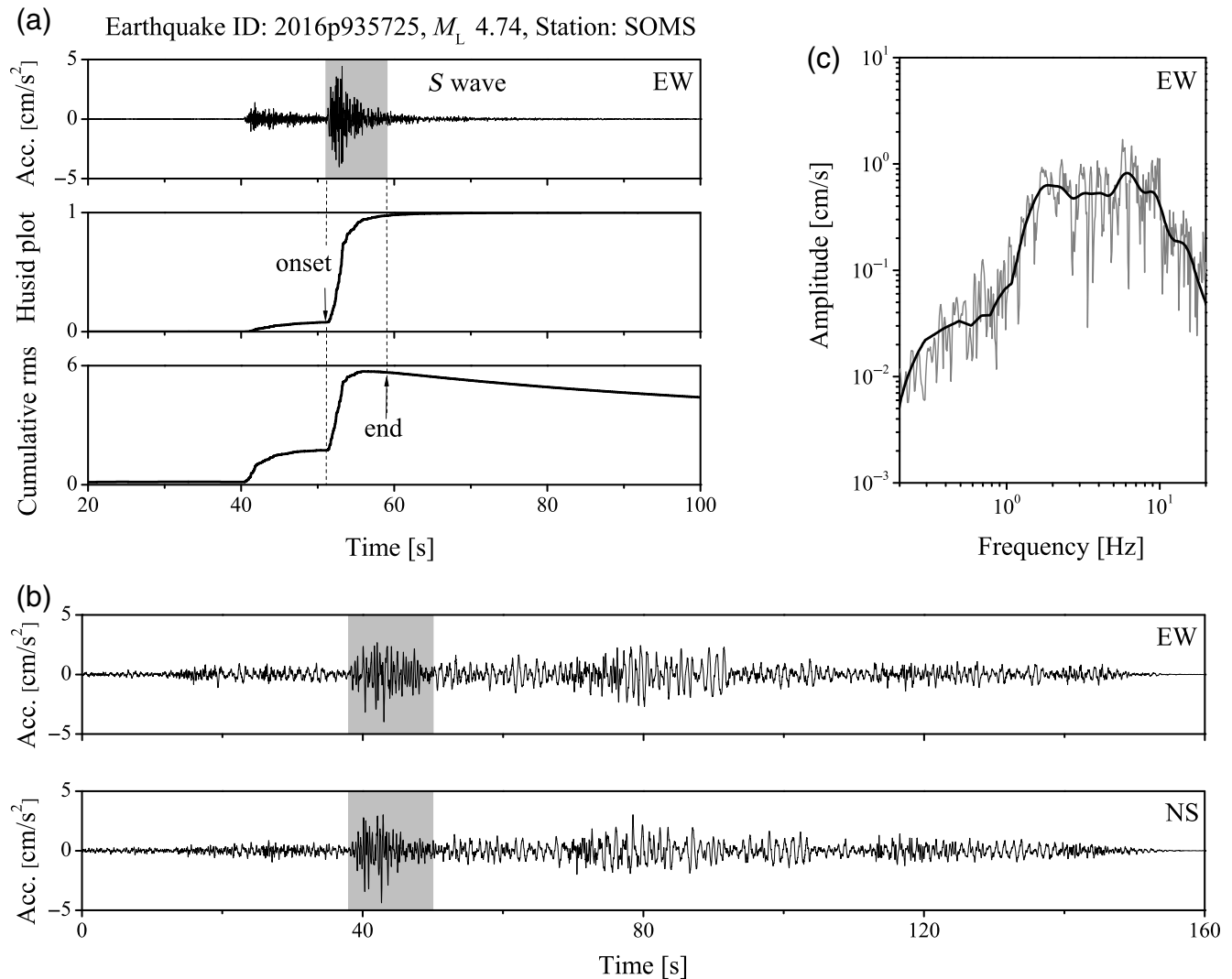


Figure 3. (a) Example illustrating how the S -wave signal is extracted according to the Husid plot and the cumulative root mean square (rms) function. (b) An example illustrating the waveforms consisting of more than one high-amplitude wave packet and the extracted S -wave window from the visual inspection. (c) The Fourier amplitude spectrum for the extracted S wave in (a) and its smoothing spectrum using the [Konno and Ohmachi \(1998\)](#) filter with $b = 20$. EW, east–west; NS, north–south.

of 0.1, 0.2, and 0.25 Hz (the high-pass corner frequencies), respectively. For the recordings including only one wave packet, the maximum S -wave window length was fixed to 20 s to exclude coda-wave effects as much as possible. For the recordings including multiple wave packets, the maximum length was fixed to 12 s to separate the different wave packets. Cosine tapers were added on both ends of the extracted S waves to eliminate truncation errors, and the length of each taper corresponded to 10% of the S -wave duration ([Hassani et al., 2011](#); [Ren et al., 2013](#)). The Fourier amplitude spectra for the tapered S waves from events with $M_L \geq 5.5$, $4.5 \leq M_L < 5.5$, and $M_L < 4.5$ were calculated and interpolated at 465 points from 0.1 to 20.0 Hz, 404 points from 0.2 to 20.0 Hz, and 384 points from 0.25 to 20.0 Hz, respectively, which were equally spaced on the logarithmic scale. Then they were smoothed using the windowing function provided by

[Konno and Ohmachi \(1998\)](#) with the smoothing parameter $b = 20$ (e.g., shown in Fig. 3c). The rms of the Fourier amplitude spectra from two horizontal S waves was adopted to represent the horizontal ground motion in the frequency domain.

Methodology

The well-known generalized inversion technique (GIT) proposed by [Andrews \(1986\)](#) was adopted to separate simultaneously the S -wave Fourier amplitude spectra into source spectra, path attenuation, and site responses. The convolution of the three contributions in the time domain can be expressed as a simple multiplication in the frequency domain,

$$O_{ij}(f, M_i, R_{ij}) = S_i(f, M_i)P_{ij}(f, R_{ij})G_j(f), \quad (1)$$

which can be transferred into a linear superposition after performing a natural logarithmic operation,

$$\ln[O_{ij}(f, M_i, R_{ij})] = \ln[S_i(f, M_i)] + \ln[P_{ij}(f, R_{ij})] + \ln[G_j(f)], \quad (2)$$

in which $O_{ij}(f, M_i, R_{ij})$ represents the acceleration Fourier amplitude spectrum at frequency f obtained at the j th station resulting from the i th earthquake with magnitude M_i , R_{ij} is the hypocentral distance, $S_i(f, M_i)$ is the source acceleration spectrum of the i th event, and $G_j(f)$ accounts for the site response of the j th station. Here, $P_{ij}(f, R_{ij})$ is the attenuation operator involving geometrical spreading, anelastic and scattering attenuation, and refracted arrivals, which can be simply expressed as

$$P_{ij}(f, R_{ij}) = \text{GS}(R_{ij}) \exp\left(\frac{-\pi f R_{ij}}{Q_S(f) \beta_s}\right), \quad (3)$$

in which $Q_S(f)$ stands for the frequency-dependent S -wave quality factor, β_s is the shear-wave velocity set to 3.7 km/s (Laske *et al.*, 2013), and $\text{GS}(R_{ij})$ represents the geometrical spreading. As is well known, a trade-off between the geometrical spreading and anelastic attenuation exists in the inversion, which could be reduced if an appropriate function of $\text{GS}(R_{ij})$ is chosen. A hinged trilinear model given by Atkinson and Mereu (1992) was used in this study, which interprets the effects of the boundary between the crust and mantle on seismic wave propagation. The model was verified by some previous studies (e.g., Atkinson and Boore, 1995; Bora *et al.*, 2015) based on a large number of strong-motion recordings, which show that geometrical spreading is not slower than R^{-1} in the local distances, while approximately equal to $R^{-0.5}$ in the regional distances. The model is expressed as

$$\text{GS}(R_{ij}) = \begin{cases} R_{ij}^{-b_1} & R_{ij} \leq R_{01} \\ R_{01}^{-b_1} R_{01}^{-b_2} R_{ij}^{-b_2} & R_{01} < R_{ij} \leq R_{02} \\ R_{01}^{-b_1} R_{01}^{b_2} R_{02}^{-b_2} R_{ij}^{-b_3} & R_{ij} > R_{02} \end{cases}, \quad (4)$$

in which $R_{01} = 1.5D$, $R_{02} = 2.5D$, $b_1 = 1.0$, $b_2 = 0.0$, and $b_3 = 0.5$. Here, D is the average depth to the Moho in the study region, which was taken as approximately 25 km according to the CRUST1.0 model (Laske *et al.*, 2013).

In this study, the singular value decomposition method was adopted to solve equation (2) (Menke, 1989). This method has been proven effective for solving the linear inversion by Parolai *et al.* (2000), and it has been adopted widely in the GIT (e.g., Oth *et al.*, 2009; Ren *et al.*, 2013). An additional degree of freedom caused by the linear dependence between the source and the site terms remains unconstrained. To eliminate this trade-off, two stations were selected as reference sites, POTS and LTZ, which are located in the Wellington and Christchurch areas, respectively (highlighted in Fig. 1).

Both stations were installed on rock (site class B in the NZS1170.5) with $V_{S30} = 1000$ m/s derived from the GeoNet database of site metadata (Kaiser, Houtte, *et al.*, 2017). The horizontal-to-vertical spectral ratios of observed recordings in the Kaikōura earthquake sequence at both stations indicate the small (<2.0) and flat site amplifications (Fig. 4). Furthermore, some studies (e.g., Bradley, Wotherspoon, and Kaiser, 2017; Bradley *et al.*, 2018) also considered the POTS station as the reference site for the site-effect analyses using the standard spectral ratio method. The site responses at both reference sites were characterized by 2.0 (considering the amplification of the free surface) at frequencies from 0.1 to 20.0 Hz.

Results

Stability of the Inversion

To verify the reliability of the inversion, the residuals between the observed spectra and the synthetic results from the product of the inverted source spectra, site responses, and path attenuation were computed and plotted versus distances and magnitude sizes, respectively, in Figure 5. The residuals, calculated as the observed minus the synthetic spectral values on a base-10 logarithmic scale, do not show obvious dependence on hypocentral distance and magnitude size. They have almost zero mean with a standard deviation of about 0.25 at all distance and magnitude bins. It shows that the GIT provides good representation of the observed spectra considered in this study.

Source Characteristics

The source displacement spectra (ratio of $(2\pi f)^2$ to source acceleration spectra) of the 148 earthquakes considered in this study are shown in Figure 6a. The spectral shapes at low to intermediate frequencies are mostly in good agreement with the omega-square source model (Brune, 1970). However, rapid decay can be observed at high frequencies. Commonly, two different models have been used to explain this rapid decay, the κ model expressed as $\exp(-\pi f \kappa)$ (Anderson and Hough, 1984) and the f_{\max} model expressed as $[1 + (f/f_{\max})^8]^{-1/2}$ (Hanks, 1982; Boore, 2003). Whereas some studies have suggested the site effect as the cause (e.g., Hanks, 1982), others have suggested the source effect (e.g., Papageorgiou and Aki, 1983). In this study, we just adopted the simple multiplicative f_{\max} filter from Boore (2003) to account for the high-frequency decay rather than considering the cause of this rapid decay. Whereas this filter was also taken into consideration in the study of Nakano *et al.* (2015), Oth and Kaiser (2014) considered the κ model to correct the rapid spectral high-frequency decay. The source displacement spectrum can be given by

$$S(f) = \frac{R_{\Theta\Phi} V F}{4\pi \rho_s \beta_s^3 R_0} \frac{M_0}{1 + (f/f_c)^2} [1 + (f/f_{\max})^8]^{-1/2}, \quad (5)$$

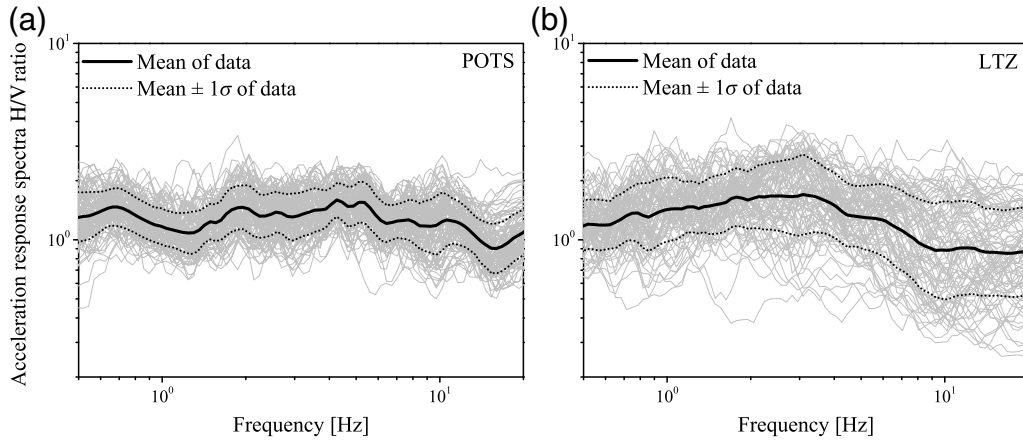


Figure 4. Horizontal-to-vertical (H/V) spectral ratios of the observed recordings at (a) POTS and (b) LTZ stations during the Kaikōura earthquake sequence. Dark solid and dotted lines represent the average and the average ± 1 standard deviation (σ).

in which M_0 and f_c are the seismic moment and corner frequency, respectively. Here, $R_{\Theta\Phi}$ accounts for the average radiation pattern over a suitable range of azimuths and take-off angles, and it was set equal to 0.55 (Boore and Boatwright, 1984). $V = 1/\sqrt{2}$ represents the proportion of S -wave energy contained in the horizontal component; F is the amplification of the free surface, fixed to 1.0 because of its consideration in the site response; $R_0 = 1$ km is the

reference distance; and ρ_s is the density near the source, which was set equal to 2700 kg/m^3 .

A grid-searching method was adopted to obtain the best-fitting seismic moment M_0 , corner frequency f_c , and high cutoff frequency f_{\max} for each event (i) under the condition that the theoretical source spectrum $S_{i,\text{theoretical}}(f)$ expressed by equation (5) showed the smallest deviations to the inverted source spectrum $S_{i,\text{inverted}}(f)$ across the entire frequency range of 0.5–20.0 Hz:

$$\sum_{m=1}^{Nf-1} \left\{ \left[\log_{10} \frac{S_{i,\text{inverted}}(f_m)}{S_{i,\text{theoretical}}(f_m)} \right]^2 \times (f_{m+1} - f_m) \right\} = \min, \quad (6)$$

in which $Nf = 324$, the total number of frequency points at frequencies from 0.5 to 20.0 Hz. To ensure a reliable result, the outputs of inversion at frequencies in 0.5–20.0 Hz range only were used in the following spectral analysis. The search scope for M_0 was determined by the scope of the moment magnitude (M_w), $M_w = M_L \pm 0.5$, according to the M_0 – M_w relationship ($\log M_0 = 1.5(M_w + 10.7)$) in $\text{dyn} \cdot \text{cm}$ units proposed by Hanks and Kanamori (1979). The values of the stress drop ($\Delta\sigma$) for small to moderate earthquakes generally vary from 0.1 to 100.0 MPa (Kanamori, 1994). Following the M_0 – f_c – $\Delta\sigma$ relationship of in equation (7) (Brune, 1970), the search scope of f_c was determined. The values of f_{\max} ranged from 1.0 to 20.0 Hz at intervals of 0.1 Hz. In this study, the step widths for M_w and f_c were fixed to 0.01 and 0.01 Hz, respectively. Figure 6b shows the best-fitting theoretical

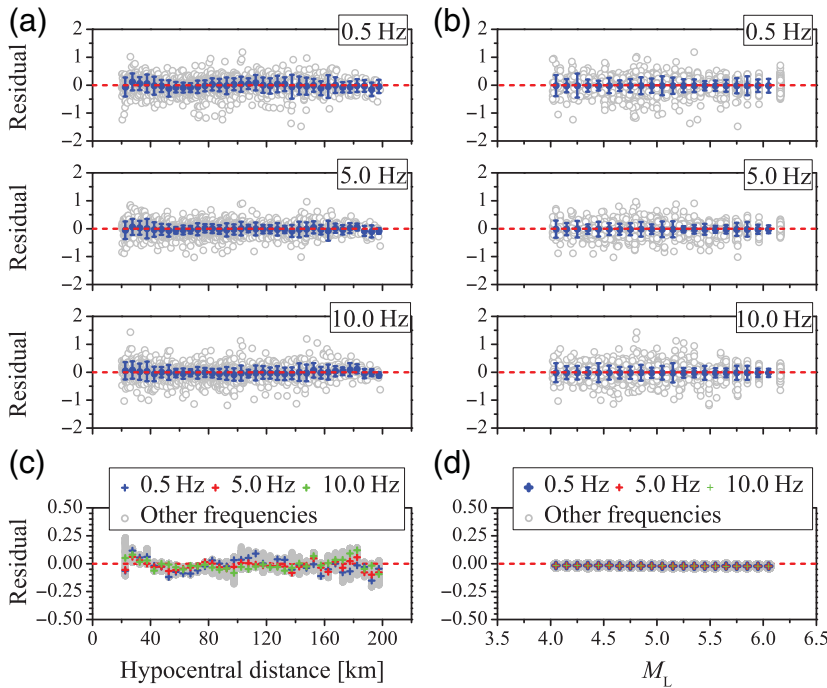


Figure 5. Residuals of the synthetic results produced by the inverted source, site, and path terms, computed as $\log_{10}(\text{observation/synthesis})$ versus (a) hypocentral distance and (b) magnitude size at 0.5, 5.0, and 10.0 Hz. Blue circles and error bars represent the average residuals and one standard deviation range for different distance and magnitude bins at the three frequencies. The average residuals for different distance and magnitude bins were computed at all frequencies from 0.5 to 20.0 Hz and plotted in (c) and (d), respectively.

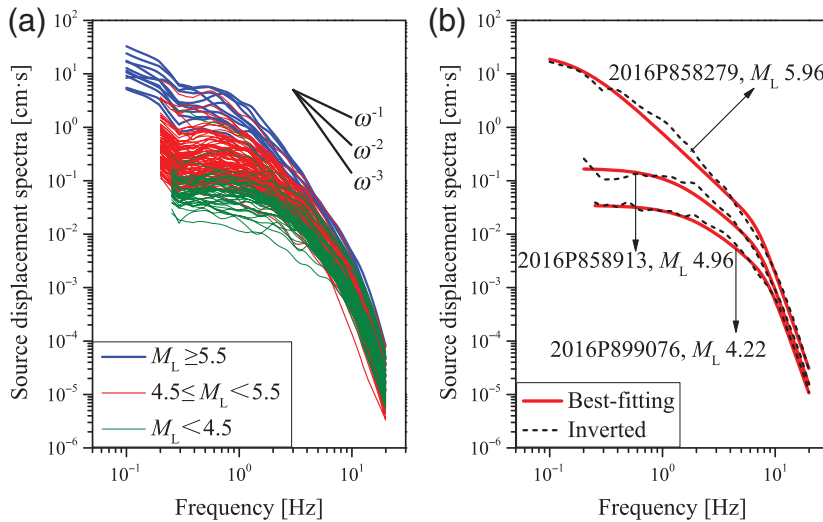


Figure 6. (a) Inverted source spectra for all 148 earthquakes considered in this study. According to the recording's filtering bandwidth (0.25–25 Hz for $M_L < 4.5$, 0.2–25 Hz for $4.5 \leq M_L < 5.5$, and 0.1–25 Hz for $M_L \geq 5.5$), the source spectra were separated into three groups considering three M_L ranges. (b) Best-fitting theoretical source spectra for three typical events at different magnitude bins.

source spectra for several typical events at different magnitude bins. Perfect matches are observed between the inverted and theoretical spectra.

Based on the optimum M_0 and f_c , the stress drop can be estimated using the following relation:

$$\Delta\sigma = \frac{7M_0}{16} \left(\frac{2\pi f_c}{2.34\beta_s} \right)^3 \quad (7)$$

(Brune, 1970). All values of M_0 , M_w , f_c , f_{\max} , and $\Delta\sigma$ for each earthquake are provided in Table S1, available in the electronic supplement to this article.

Figure 7a shows scatter plots of M_w estimated in our study against M_L values for all 148 earthquakes. The orthogonal least-squares regression (OSR) yielded an empirical conversion relationship between M_w and M_L ,

$$M_w = (0.9586 \pm 0.0494)M_L + (0.0645 \pm 0.2278). \quad (8)$$

Another two methods, standard least-squares regression (SR) and inverted standard least-squares (ISR) regression, were also used to test which regression is the best. The results show that the OSR is midway between the SR and ISR, indicating the OSR method performs best (Castellaro and Bormann, 2007). Equation (8) was compared with the conversion relationship between M_w and M_L proposed by Ristau *et al.* (2016), as shown in Figure 7a, presenting perfectly consistent results given by both studies. Moreover, Figure 7b shows that the estimated M_w are consistently smaller than M_L with an average of ~ 0.13 , which has the same tendency given by Ristau *et al.* (2016) with an average deviation of 0.15.

The scaling characteristics for the Kaikōura earthquake sequence in the form of the M_w - f_c plot are shown in Figure 8a. The values of M_0 and f_c vary from 6.68×10^{14} to 7.67×10^{17} N·m and from 0.19 to 2.61 Hz, respectively. If earthquakes follow self-similarity, the value of M_0 is approximately inversely proportional to the cube of f_c , that is, $M_0 \propto f_c^{-3}$, which also means the stress drop is constant and independent of magnitude size (Aki, 1967). Studies by Allmann and Shearer (2009), Oth *et al.* (2010), and Zhao *et al.* (2011), among others, all confirmed the self-similarity of global earthquakes. However, some other studies have obtained conflicting results, in which self-similarity is broken down in some specific earthquake sequences (e.g., Tusa *et al.*, 2006; Drouet *et al.*, 2010; Mandal and Dutta, 2011; Oth, 2013; Pacor *et al.*, 2016). Kanamori and Rivera (2004) proposed the parameter

ε in the formula $M_0 \propto f_c^{-(3+\varepsilon)}$ to reflect quantitatively the deviations from self-similarity. In the case of $\varepsilon = 0$, self-similarity is followed perfectly, but the case of $\varepsilon > 0$ ($\varepsilon < 0$) indicates an increasing stress drop with increasing (decreasing) magnitude. In this study, a value of $\varepsilon = 0.02 \pm 0.08$ was determined from the regression analysis, implying sound self-similarity for the Kaikōura earthquake sequence within the magnitude M_L 4.02–6.16 range. Interestingly, in the 2010–2011 Canterbury earthquake sequence (shown in Fig. 1), which occurred just southwest of this sequence, it was also confirmed that the stress-drop scaling with earthquake size was nearly self-similar (Oth and Kaiser, 2014).

The $\Delta\sigma$ values for the Kaikōura earthquake sequence follow a lognormal distribution, as shown in Figure 8b, and they vary predominantly from 0.2 to 6.0 MPa with a logarithmic mean of 1.25 MPa. These values are overall lower than the 2010–2011 Canterbury earthquake sequence with a logarithmic mean of ~ 5 MPa, as shown in Figure 8a. The mean stress drop of the Kaikōura earthquake sequence is also lower than the median of global interplate earthquakes, 3.31 MPa given by Allmann and Shearer (2009). Furthermore, no evidence was observed regarding the dependence of the stress drop on either magnitude or focal depth, as shown in Figure 8c,d.

In the Kaikōura earthquake sequence, most aftershocks occurred northeast of the main event epicenter, located generally within the horizontal projection of the second segmentation of the fault rupture planes provided by U.S. Geological Survey (USGS) (see Data and Resources, highlighted in Figure 1 by the blue box). Although more elaborate kinematic fault models that match the surface rupture characteristics were provided by Hamling *et al.* (2017), the simple USGS model was used to provide a referenced geographic location to clearly delineate the spatial distribution of the stress-drop

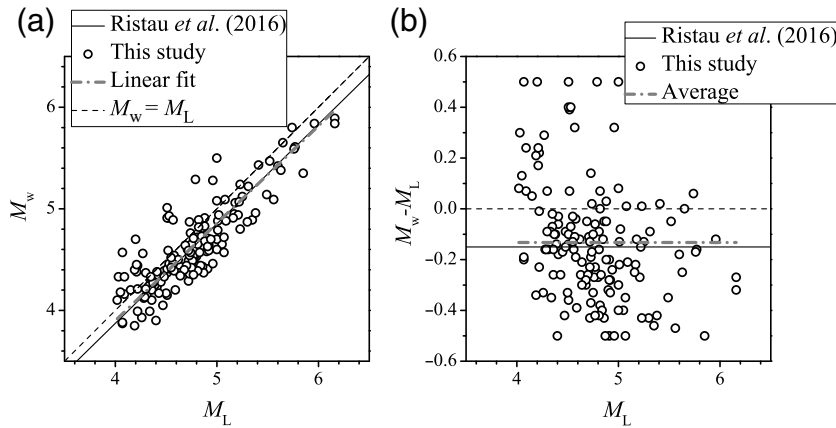


Figure 7. (a) Moment magnitude M_w estimated in our study versus M_L derived from GeoNet. The dashed-dotted line represents the best-fit orthogonal least-squares linear regression. The solid line represents the conversion relationship between M_w and M_L (with intercept 0.05 and slope 1.02) proposed by Ristau *et al.* (2016). (b) Difference between M_w and M_L versus M_L , showing M_w is ~ 0.13 magnitude units smaller than M_L on average, close to ~ 0.15 as proposed in the study of Ristau *et al.* (2016), indicated by the solid line.

values for dense aftershocks, independent of the fault model used. We simply divided these events into two parts: part A is a cluster of events in the north of the rupture plane, and part B includes events in the south, as shown in Figure 1. The tension spline interpolation method was used to derive the contours, as shown in Figure 9. It can be observed that events with larger stress drop ($\Delta\sigma > 4.5$ MPa) are all located in part A, and events located in part B have stress-drop values almost all less than 3.0 MPa. The $\Delta\sigma$ values for the events of part A are generally higher than for the events of part B, implying systematic lateral variations, which have also been observed in some other earthquake sequences, for example, the 2010–2011 Canterbury earthquake sequence (Oth and Kaiser, 2014) and the 2008–2013 Wenchuan earthquake sequence (Wang *et al.*, 2018).

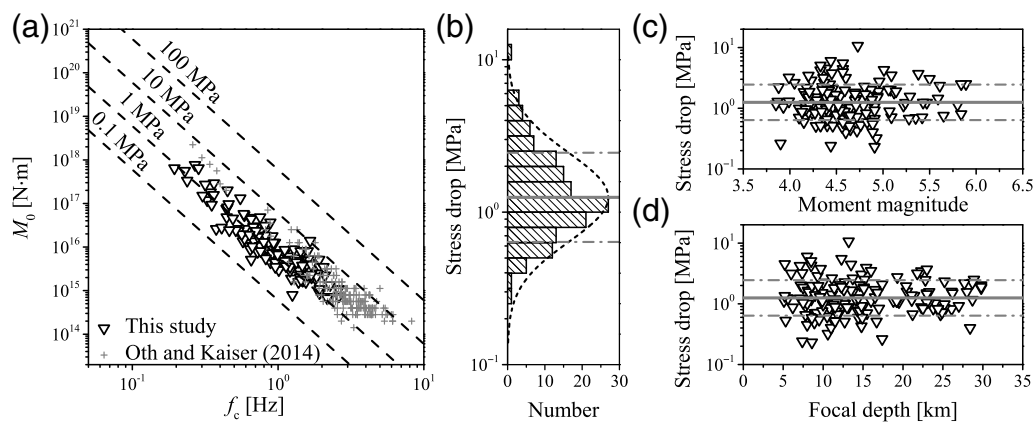


Figure 8. (a) Plots of the seismic moment M_0 versus corner frequency f_c . Dashed lines represent the theoretical relationship between M_0 and f_c for various stress-drop levels, as indicated on the top of each line. The M_0 – f_c plots for the 2010–2011 Canterbury earthquake sequence provided by Oth and Kaiser (2014) were compared with our results. (b) Histogram of the stress-drop values on the base-10 logarithmic scale, and the best-fitting lognormal distribution function; (c) stress drop versus moment magnitude; and (d) stress drop versus focal depth. Solid and dashed-dotted lines in (b)–(d) represent the logarithmic mean of the stress drop and its standard deviation.

Site Responses

The site-response functions at frequencies ranging from 0.5 to 20.0 Hz for the 126 strong-motion stations in this study, obtained by the GIT, are provided in ⑤ Figure S1. The bootstrap analysis proposed by Oth *et al.* (2008, 2011) was performed in this study to calculate the standard deviation of site response. A total of 375 recordings, accounting for approximately 15% of the total recordings, were removed randomly from the dataset, and the remaining ones were assembled as a new dataset used in the inversion. The site responses calculated from repeated procedures in 100 times were used to derive the standard deviations.

We compared the site-predominant frequencies identified by the site responses inverted in this study with those calculated by a multiplicative inverse of the fundamental site periods (T_{site}) provided by the GeoNet database of site metadata (Kaiser, Houtte, *et al.*, 2017), as shown in Figure 10. In view of the shapes of the site-response functions versus frequency, stations were classified into three categories for estimating the fundamental frequency. In the first category, the site-response function has only a single peak, and the frequency at this peak was identified as the fundamental frequency. In the second category, more than one peak could be observed in the site-response function, and the smaller peak frequency was identified as the fundamental frequency. In the third category, the site-response function appears approximately flat, implying the fundamental frequency is unidentifiable. The site parameters of the GeoNet database, including T_{site} and V_{S30} , were classified into three categories: Q_1 , Q_2 , and Q_3 , according to quality assessments corresponding to

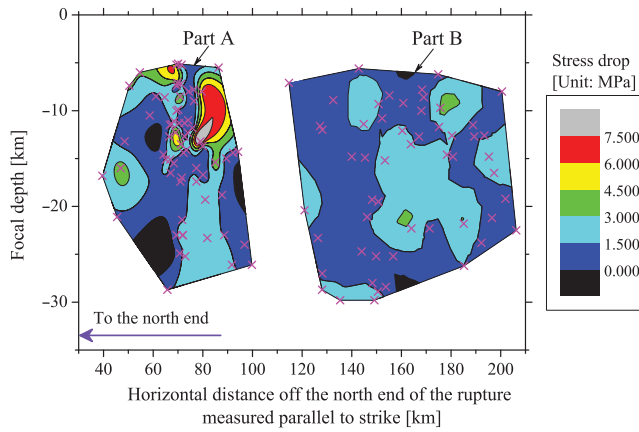


Figure 9. Spatial distributions of stress-drop values for events in the north cluster (Part A) and in the south cluster (Part B) defined in Figure 1. Each event was located by its focal depth and the horizontal distance off the north end of the second segmentation of the ruptured plane (provided by the USGS) measured parallel to strike. Crosses indicate the epicenters.

approximate uncertainties of 10%, 10–20%, and >20%, respectively. A total of 48 stations with respect to categories Q_1 and Q_2 were included in our study. According to the above-mentioned criteria, 28, 7, and 13 were classified as the first, second, and third categories, respectively. The comparison in Figure 10 shows that the site-predominant frequencies estimated by the two studies are soundly consistent, indicating partially the reliability of the estimations of the site responses by the GIT in this study.

Among the 126 strong-motion stations used in this study, the site classes of 118 stations are provided by the GeoNet database of site metadata (Kaiser, Houtte, et al., 2017). They are classified into four types according to the definitions of site classification in the New Zealand design standard NZS1170.5, comprising 28 class B sites (soft rock), 23 class C sites (shallow soil), 58 class D sites (deeper or soft soil), and 9 class E sites (very soft soil). The mean site responses averaged over all stations classified as the same site class and their standard deviations are plotted in Figure 11. Compared with Kaiser et al. (2016; see their fig. 3), which is an ongoing study of Oth and Kaiser (2014), both studies show similar tendency of the estimated average site amplifications for classes D and E but different tendency for classes B and C. Our study frames a larger area than Kaiser et al. (2016), and regional differences of site amplifications for classes B and C are probably due to topographic or material effect (or both). We note that double times free surface amplification is included in the site responses in our study, which would cause relatively large standard deviations. The standard deviations illustrate the larger variations of site amplification for class C and smaller variations for class E, the same as identified by Kaiser et al. (2016). The predominant frequency shifts from high to low when the site class varies from B to E, that is, softer soil produces lower predominant frequencies. In addition, the site response

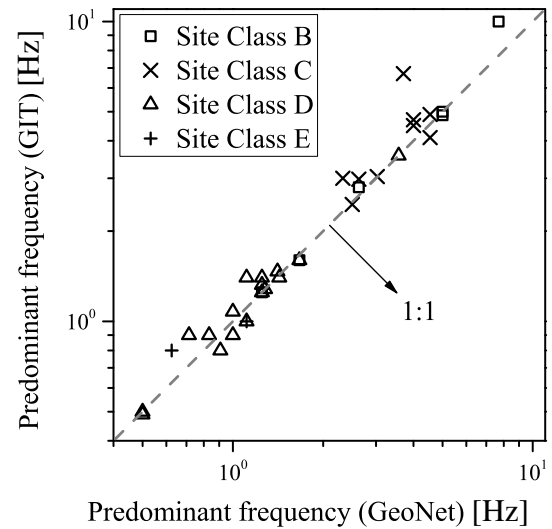


Figure 10. Comparisons of the predominant frequencies identified by the inverted site responses with those calculated by a multiplicative inverse of the fundamental site periods provided by the GeoNet database of site metadata (Kaiser, Houtte, et al., 2017). The dashed line represents the 1:1 relationship. GIT, generalized inversion technique.

exhibits larger amplification at the low-frequency band but smaller amplification at the high-frequency band when the soil becomes much softer. These observations are in accordance with the common sense in the earthquake engineering community.

To detect the correlations between the site amplification and the site parameters, for example, V_{S30} and T_{site} , 24 stations with credible values of V_{S30} (quality levels of Q_1 and Q_2) and 50 stations with credible values of T_{site} (quality levels of Q_1 and Q_2) were included in the analysis, respectively. Taking 0.5 Hz as an example in Figure 12a,b, good correlations between the site amplification and either V_{S30} or T_{site} can be observed clearly with both able to be expressed as a linear relationship:

$$\ln(\text{Amp.}) = a + b \ln(V_{S30}) \quad (9)$$

and

$$\ln(\text{Amp.}) = a + b \ln(T_{\text{site}}), \quad (10)$$

in which Amp. represents the site (de-)amplification at each frequency. The linear correlation coefficients at each frequency from 0.5 to 20.0 Hz for the Amp.– V_{S30} and Amp.– T_{site} regressions were computed, and they are shown in Figure 12c. The Amp.– V_{S30} relationship shows negative correlation at the low-frequency band but positive correlation at the high-frequency band. However, the Amp.– T_{site} relationship follows the opposite trend. Moderate correlations, represented by the ranges of correlation coefficients from 0.5 to 0.8 and from –0.8 to –0.5, can be observed clearly at the low-frequency band (<~3.0 Hz) for both relationships. Weak correlations are also evident at the high-frequency band (>~8.0 Hz),

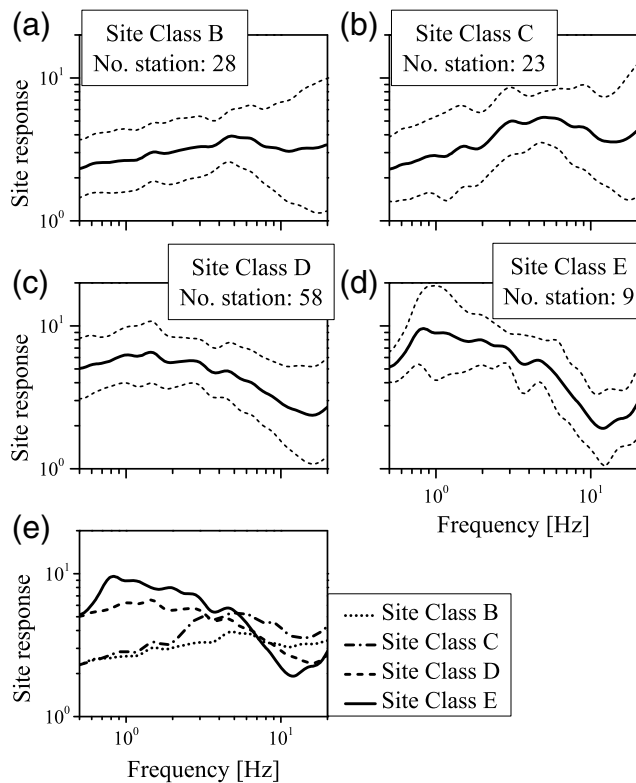


Figure 11. Mean site amplification for each site class (B–E) according to the New Zealand design standard NZS1170.5. (a)–(d) Geometric mean (solid line) and one standard deviation variation (dashed lines); (e) comparison of average amplification functions across site classes.

but the relationship is almost independent at the intermediate-frequency band (~ 3.0 – 8.0 Hz). Actually, negative correlation between the site amplification and V_{S30} at the low-frequency band has been reported in many studies, for example, at a band of 0.5 – 2.5 Hz by Dutta *et al.* (2003), 0.4 – 1.0 Hz by Hassani *et al.* (2011), and 0.5 – 1.0 Hz by Tsuda *et al.* (2010). In addition, the independence at the intermediate-frequency band has also been reported previously, for example, at a band of 3.0 – 7.0 Hz by Dutta *et al.* (2003) and 2.5 – 6.0 Hz by Hassani *et al.* (2011). According to the least-squares regression analysis, the values for the slope (b) and the intercept (a) for the relationships of $\text{Amp.} - V_{S30}$ (equation 9) and $\text{Amp.} - T_{\text{site}}$ (equation 10) were obtained, as shown in Figure 12d and 12e, respectively. It should be noted that the regressions were performed only within the frequency band (Fig. 12c) at which both $\text{Amp.} - V_{S30}$ and $\text{Amp.} - T_{\text{site}}$ had moderate correlations. Coefficients a and b in the relationship of $\text{Amp.} - V_{S30}$ vary from 5.75 to 10.89 and from -1.65 to -0.74 at the low-frequency band (0.5 – 3.0 Hz), respectively, which are approximately in good agreement with those provided by Dutta *et al.* (2003).

Note the dense clustering of stations near Wellington and Christchurch that allowed us to investigate the site effects on both regions. The Christchurch city is situated on a sedimentary fan deposit with the volcanic rock of Banks

Peninsula located to the southeast. The surface geology within the city consists primarily of the Springston Formation (Holocene alluvial gravels, sand, and silts) and the Christchurch Formation (dune and beach sands) (Brown and Weeber, 1992). In the wake of the 2010–2011 Canterbury earthquake sequence, the city has aroused great concern among earthquake engineering community because of significant site effects excited by extreme ground motions, including the widespread liquefaction, salient sedimentary basin effects, topographic effects, and so on (Bradley and Cubrinovski, 2011; Cubrinovski *et al.*, 2011; Fry *et al.*, 2011; Mucciarelli, 2011; Smyrou *et al.*, 2011; Bradley, 2012, 2016; Wotherspoon, Orense, Green, *et al.*, 2015; Kaiser *et al.*, 2016). The site effects exhibited in the Kaikōura earthquake sequence would also be of great interest.

The tension spline interpolation method was used to derive the contour map of the average site amplification over frequencies of 0.5 – 3.0 Hz, as shown in Figure 13a. The site amplifications in the south of Christchurch (~ 3 – 5) were smaller than the north (~ 6 – 8), which might be inferred as the result of shallow basement rock depth in the southern Christchurch associated with uplift during Miocene volcanism (Wotherspoon, Orense, Bradley, *et al.*, 2015).

A majority of stations situated on the Christchurch sedimentary basin are classified as class D and E sites (see Fig. 13a) covered by the soft near-surface soils ($V_{S30} < 250$ m/s). Only four stations are classified as class B and C sites. They are stations HVSC and MENS (class C) located near the north edge of the Port Hills and stations HUNS and MTPS (class B). The site amplifications of these stations shown in Figure 13a were all plotted in Figure 13b. For both class B sites, the flat amplification function shows weak site responses (~ 3.0 , including double-times free surface amplification). The larger amplifications at frequencies from 2 to 8 Hz, exhibited at station HVSC than at station MENS, could be interpreted by the basin-edge effect, which was also observed in the 13 June 2011 M_w 6.0 Christchurch earthquake (Bradley, 2016). The amplifications at frequencies lower than ~ 3.0 Hz for the stations (class D and E sites) within the sedimentary basin are consistently larger than the southeastern stations (class B and C sites), which illustrates the effects of the thick sequence of soil layer, previously observed in the Canterbury seismic sequence (Bradley and Cubrinovski, 2011; Bradley, 2012).

It should be noted that stronger amplifications appeared in the Christchurch Central Business District (CBD), that is, close to stations CBGS, CCCC, REHS, and MORS (see Fig. 13a). The amplifications at low frequencies for these four stations are larger than the average values over all class D and E sites, as shown in Figure 13b. This might be a reason why the ground motions observed in 0.5 – 1.75 s period range close to the natural vibration periods of the 5- to 20-story reinforced concrete (RC) buildings exceeded the 2500-yr return period design level in the Christchurch CBD in the 2011 M_w 6.2 Christchurch earthquake (Kam *et al.*, 2011; Kaiser *et al.*, 2012). The extreme ground motions caused severe

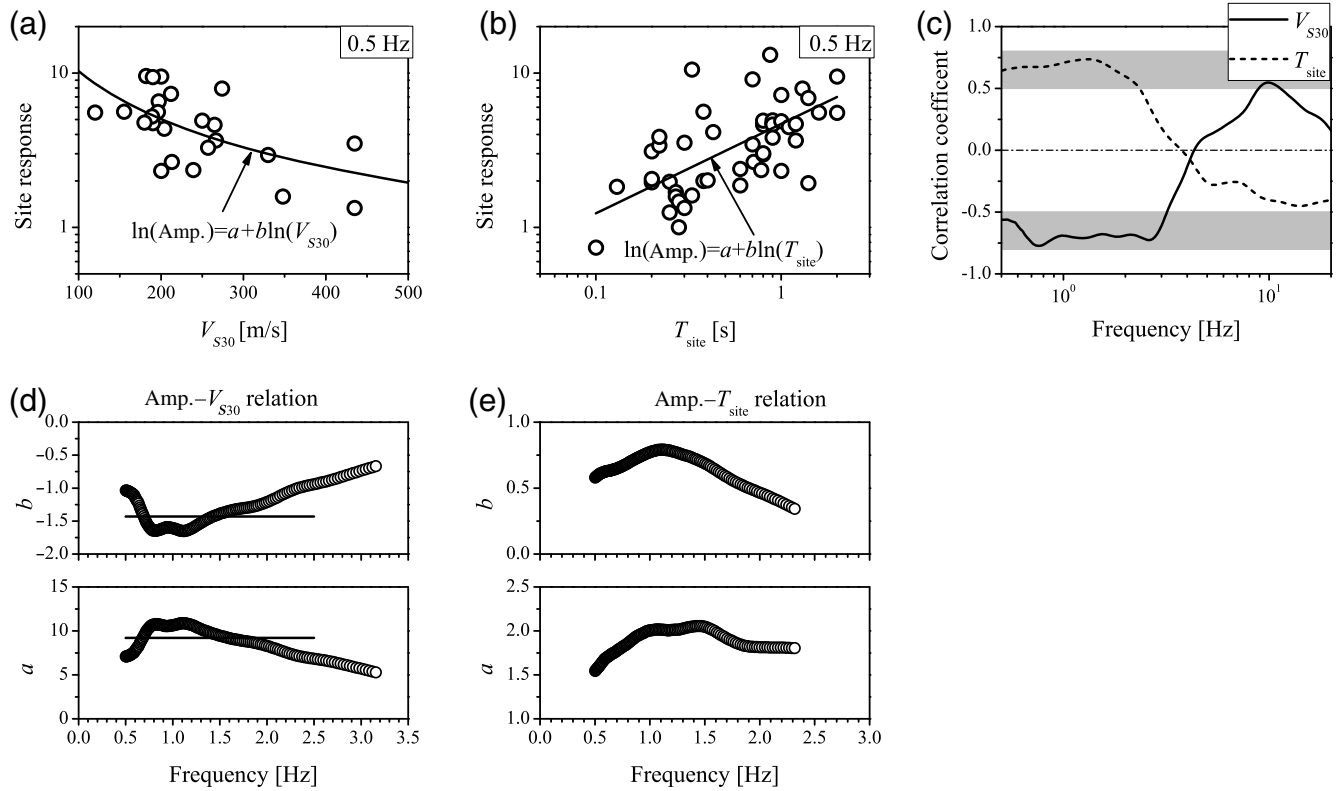


Figure 12. Site amplification (Amp.) at 0.5 Hz versus (a) V_{S30} and (b) fundamental site period T_{site} . Solid lines indicate the best-fitting relationships between the two parameters. (c) Linear correlation coefficients for the linear regressions of Amp.- V_{S30} and Amp.- T_{site} . Shaded areas indicate the ranges of correlation coefficients from 0.5 to 0.8 and from -0.8 to -0.5 corresponding to the moderate correlation. Regression coefficients a and b for the relationships of (d) Amp.- V_{S30} and (e) Amp.- T_{site} were obtained by least-squares regression analysis. Solid lines indicate the regressed values of a and b in the relationship between the average site amplification over frequencies from 0.5 to 2.5 Hz and V_{S30} given by [Dutta et al. \(2003\)](#).

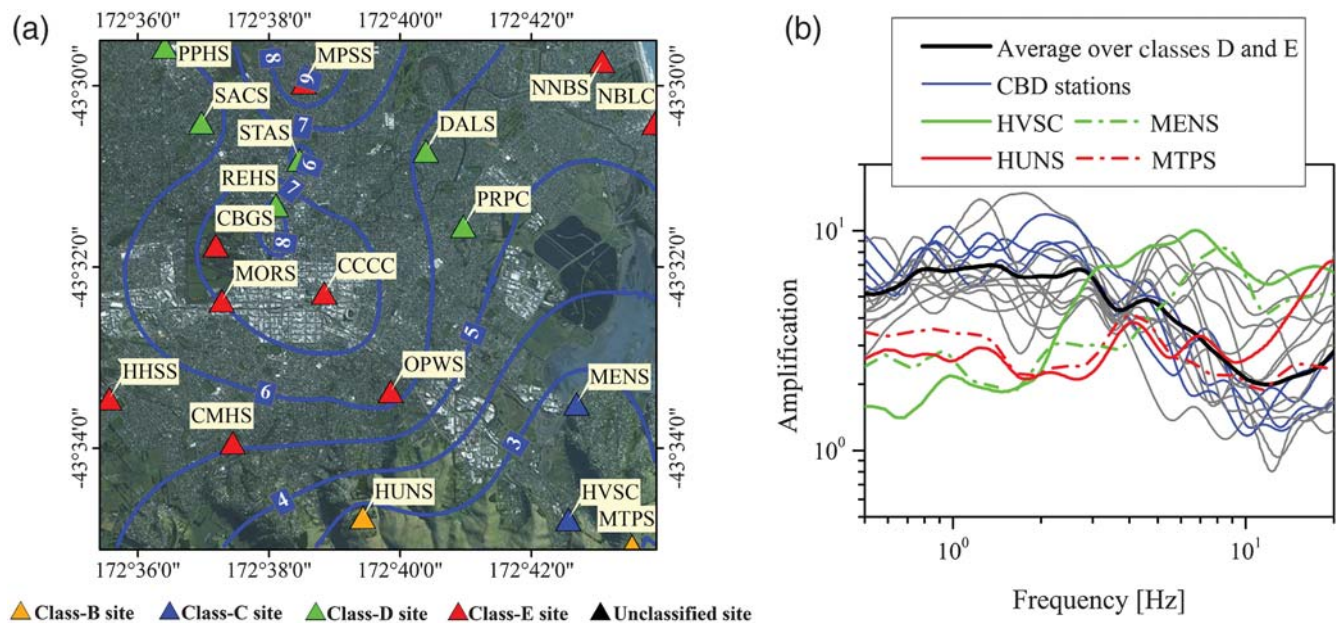


Figure 13. (a) Contours (blue lines) for average site amplification at low-frequency band (0.5–3.0 Hz) in the Christchurch city. Numbers lying on the lines indicate the amplification values. Triangles of different colors represent the different site classes provided by the GeoNet database of site metadata ([Kaiser, Houtte, et al., 2017](#)). (b) The site-response functions at stations shown in (a).

damage to a large number of RC buildings in the Christchurch CBD, as reported by Kam *et al.* (2011), and the high ratios of building damage around stations REHS and CCCC (Iizuka *et al.*, 2011).

In central Wellington, only 60 km to the north of the causative faults of the Kaikōura mainshock, the site effects of 14 strong-motion stations were analyzed in detail for the potential needs of seismic design. The relatively high seismic risk in this region was unambiguous because of the dense population and infrastructure in close proximity to several seismogenic sources, especially the northwestern active Wellington fault dividing the Western hills and the central Wellington region. As for Christchurch city, the contour for the average site amplification over frequencies of 0.5–3.0 Hz was calculated using the tension spline interpolation method, as shown in Figure 14a. It exhibits an obvious trend of amplification gradually increased from the western highlands to the eastern coasts in the north (north to 41°17'0" S). The spatial variation of site amplification shows approximate consistency with the contours of soil depth to bedrock and site period (see maps 4 and 6 in appendix 3 of Semmens *et al.*, 2010), indicating larger site amplification in regions with deeper soil layers.

According to the geological map provided by Semmens *et al.* (2010), the central Wellington region comprises greywacke bedrock, Pleistocene and Holocene alluvial, colluvial and shallow marine deposits, and staged reclamation using both hydraulic and quarry fill. According to the GeoNet database of site metadata (Kaiser, Houtte, *et al.*, 2017), two rock stations, POTS and WEL, were classified as class B sites. Station PIPS located on the reclamation overlying the alluvial deposits was classified as class E site. Two stations also located on the reclamation (TEPS and FKPS) and three stations located on alluvial deposits (TFSS, VUMS, and WEMS) were classified as class D sites. Station TRTS located on the south was classified as class C site. The site classes for the remaining five stations were unclassified. The site amplifications of these stations shown in Figure 14a were all plotted in Figure 14b–d.

Figure 14b illustrates the weak and flat site amplifications for both rock sites, ~ 2.0 at station POTS (the reference station in our study) and ~ 3.5 at station WEL. For this reason, the station POTS recorded relatively small amplitudes of ground motion during the Kaikōura mainshock (Kaiser, Balfour, *et al.*, 2017). The class C site (station TRTS) exhibits larger amplifications than both rock sites at frequencies from 3 to 7 Hz.

The amplifications at the three reclaimed sites (stations PIPS, TEPS, and FKPS) indicate notable differences, as shown in Figure 14c. The largest amplifications occur at station PIPS across the entire frequency range of 0.5–20.0 Hz. Compared with the station FKPS, the station TEPS shows higher amplifications at low frequencies below ~ 2.0 Hz but shows lower amplifications at high frequencies over ~ 2.0 Hz. As described by Bradley, Wotherspoon, and Kaiser (2017) and Bradley *et al.* (2018), the station PIPS generally

recorded the strongest spectral amplitudes in central Wellington in the Kaikōura earthquake; the station FKPS recorded the higher short-period ($< \sim 0.7$ s) but smaller long-period ($> \sim 0.7$ s) spectral amplitudes than the observations at station TEPS. The variations of site amplification among the three stations mirror the observed spectral amplitudes in the Kaikōura earthquake and might be related to the sediment thicknesses, which were inferred to be approximately 60 m at FKPS, 120 m at TEPS, and ~ 200 m at PIPS (Semmens *et al.*, 2010).

For the three stations located on alluvial deposits, station WEMS exhibits smaller site amplifications than the other two stations (TFSS and VUWS), as shown in Figure 14d. Coincidentally, the lowest spectral amplitudes at periods less than 2.0 s were observed at this station (Bradley, Wotherspoon, and Kaiser, 2017; Bradley *et al.*, 2018).

Quality Factor Q_S

Figure 15 shows the inverted frequency-dependent quality factor Q_S at each frequency of 0.5–20.0 Hz and the best-fitting linear relationship in the logarithmic scale according to a common functional form of $Q_0 f^n$, $Q_S(f) = 130.87 f^{1.07}$ in our study. The regression correlation coefficient reached a remarkable value of 0.99, implying that a stable inversion was achieved for each frequency.

Each value of Q_S shown in Figure 15 is an integrated result from a simultaneous separation of all recordings in the dataset. Here, we individually separated the Q_S value at each frequency of 0.5–20.0 Hz from each recording using equation (2). The inverted source spectrum for each earthquake shown in Figure 6 and the site-response function for each station provided (see $\text{\textcircled{E}}$ Fig. S1) were substituted for $S_i(f, M_i)$, and $G_j(f)$, respectively, in equation (2). For each recording of the dataset, the derived Q_S values over the entire frequency range of 0.5–20.0 Hz were regressed individually using the same functional form of $Q_0 f^n$. Figure 16 plots the distributions of Q_0 versus R and n versus R . The binned means of the Q_0 and n values were calculated for the uniformly logarithmic scale from $R = 20$ to 200 km. Only Q_0 and n values derived from the regressions with correlation coefficients > 0.8 are included in this figure. Figure 16 shows that Q_0 and n are dependent on R for $R < \sim 100$ km but approximately constant for $R > \sim 100$ km. This could be explained by the well-known theory that seismic waves propagating in the upper crust with various media dominate the ground motions in the near field, but seismic waves propagating in the deeper crust with stable crustal structures dominate the ground motions in the far field. In addition, the constant values of Q_0 and n for R from 100 to 200 km indicate little lateral variation of Q_S in our study region.

To investigate the potential regional dependence of Q_S , values of Q_0 and n derived from the strong-motion recordings obtained at stations located within the Wellington and Christchurch regions were selected. For simplicity, we call them Wellington Q_0 (or n) and Christchurch Q_0 (or n), which

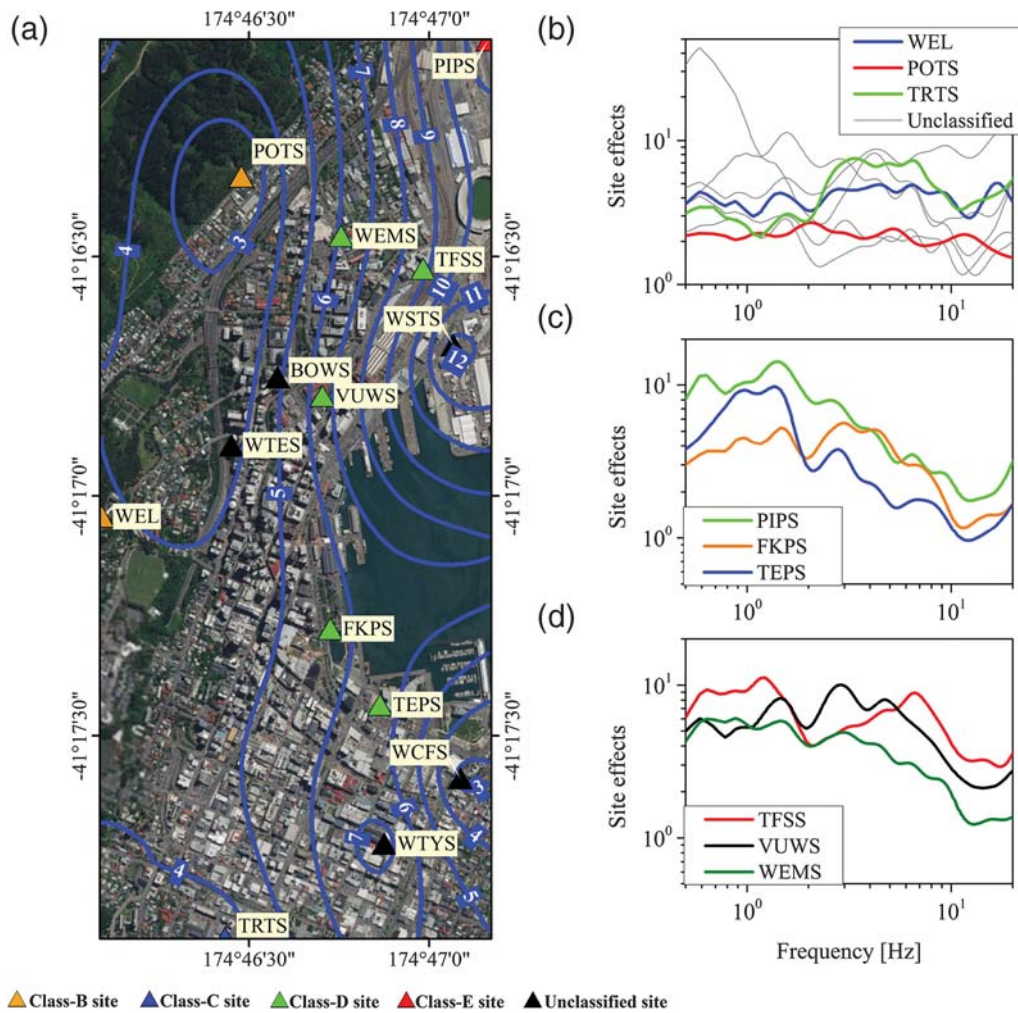


Figure 14. (a) Contours (blue lines) for average site amplification at low-frequency band (0.5–3.0 Hz) in Wellington city. Numbers lying on the lines indicate the amplification values. Triangles of different colors represent the different site classes provided by the GeoNet database of site metadata (Kaiser, Houtte, *et al.*, 2017). (b) Site amplification functions at rock (WEL and POTS), class C (TRTS), and unclassified site stations. (c) Site amplification functions at three reclaimed sites. (d) Site amplification functions at three alluvial-deposit sites.

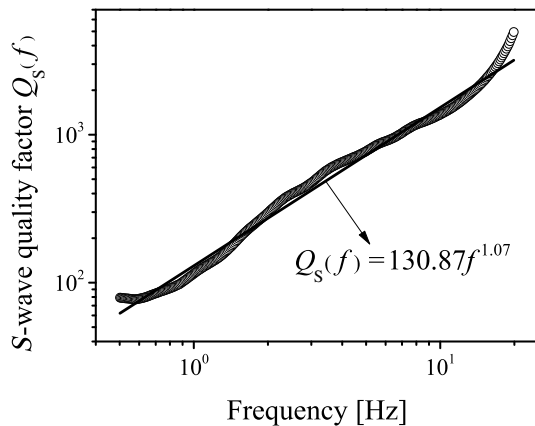


Figure 15. Frequency-dependent S -wave quality factor Q_s . The solid line represents the least-squares regression at frequencies of 0.5–20.0 Hz.

represent the anelastic attenuation characteristics of the seismic waves propagating from the sources to the southern North Island and northeastern South Island of New Zealand, respectively. The binned means of Wellington Q_0 (or n) and Christchurch Q_0 (or n) were also calculated, as shown in Figure 16. Both are comparable at each distance bin, implying no significant regional dependence of anelastic attenuation in our study region. Large regional variations in physical properties (e.g., crustal velocity) do occur across New Zealand (Eberhart-Phillips *et al.*, 2010; Fry *et al.*, 2014). However, our study region consists mainly of the northeastern South Island and the southern end of the North Island. The basement terranes for this region are predominantly constrained by the Torlesse metasediments of continental origin that have all been accreted to the Gondwana crust (Mortimer, 2004). The tectonics is dominated by the strike-slip Marlborough fault system and the contractional North Canterbury fault zones, as well as the Hikurangi subduction margin in the southern North Island (Litchfield *et al.*, 2014). The

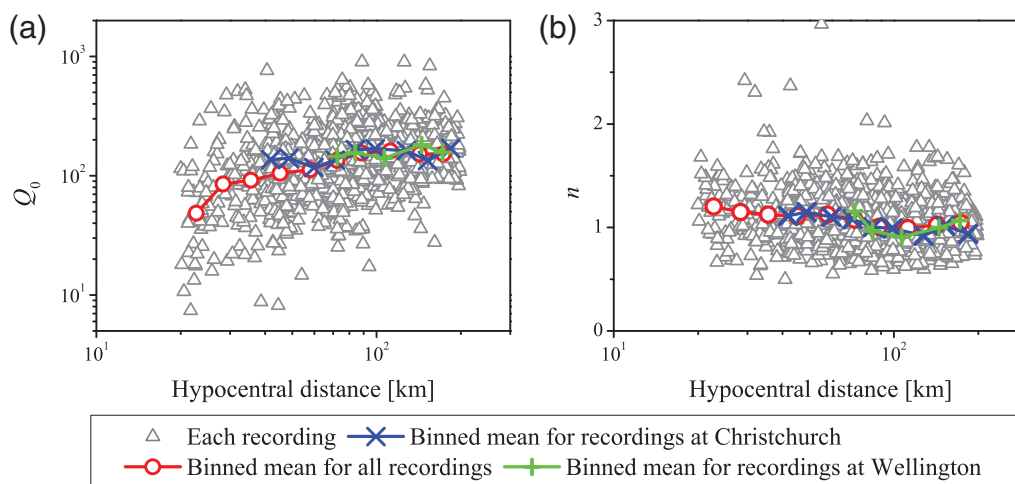


Figure 16. Values of (a) Q_0 and (b) n derived from each recording of the dataset according to equation (2) in which the source and site terms are determined using the previously inverted results. The binned means of Q_0 and n derived from the strong-motion recordings obtained at stations located within the Wellington and Christchurch regions are highlighted.

low-velocity crustal structure surrounding the study region shows some variation, confirmed in previous studies (e.g., Eberhart-Phillips and Bannister, 2010; Eberhart-Phillips *et al.*, 2010; Fry *et al.*, 2014). However, it could be acceptable that no significant regional dependence of anelastic attenuation was observed in our study region.

Conclusion

The GIT was adopted to simultaneously separate the terms of source, site, and path from the S -wave amplitude spectra of 2445 strong-motion recordings, which were obtained at 126 GeoNet strong-motion stations in the 148 aftershocks of the 2016 Kaikōura earthquake. First, the stability of the inversion was validated. Then the inverted results were used to investigate the source-scaling properties, site effects particularly in the regions of Wellington and Christchurch, and regional dependence of path attenuation. Some major conclusions could be drawn.

1. The values of seismic moment (M_0), moment magnitude (M_w), corner frequency (f_c), and stress drop ($\Delta\sigma$) were derived for each aftershock considered in this study. The values of M_0 and f_c varied from 6.68×10^{14} to 7.67×10^{17} N · m and from 0.19 to 2.61 Hz, respectively, and M_0 was found to be inversely proportional to the cube of f_c , implying that the Kaikōura aftershocks soundly followed the earthquake self-similarity. This study only covered small and moderate earthquakes with M_L ranging from 4.02 to 6.16. Caution needs to be exercised when self-similarity is assumed beyond this magnitude range. The values of stress drop predominantly varied from 0.2 to 6.0 MPa with a logarithmic mean of 1.25 MPa, which is significantly lower than those determined for the 2010–2011 Canterbury earthquake sequence (i.e., ~ 5 MPa; Oth and Kaiser, 2014)
2. The site-response functions for 126 stations considered in this study were estimated. The site-predominant frequencies identified by the site-response functions were soundly consistent with the multiplicative inverses of the fundamental site periods (T_{site}) at 35 stations within categories Q_1 and Q_2 for T_{site} provided by the GeoNet database of site metadata (Kaiser, Houtte, *et al.*, 2017). Linear relationships between the site amplification and site characteristic parameters, V_{S30} and T_{site} , at each frequency point of 0.5–20.0 Hz were regressed. The results showed that the correlation of site amplification with both parameters was moderate at the low-frequency band ($< \sim 3.0$ Hz), weak at the high-frequency band ($> \sim 8.0$ Hz) but almost independent at the intermediate frequency band (~ 3.0 – 8.0 Hz).
3. Site amplifications in the Wellington region exhibited strong correlation with the geological and geotechnical characterization, for example, the depth of soil deposit. Larger amplifications appeared in regions with deeper soil. Contour maps of site amplification in the Wellington and Christchurch regions exhibited considerable spatial variations. Analyses of some typical stations showed largely frequency-dependent variations of site amplifications among stations with different site classes, which could explain their observed spectral amplitudes in the mainshock (Bradley *et al.*, 2018). Strong site amplification appeared in the Christchurch CBD, which consistent with previous studies, could explain the severe damage caused in this area in the 2011 M_w 6.2 Christchurch earthquake.
4. The inverted S -wave quality factor was significantly frequency dependent, and it was regressed by a functional

and lower than the median value for global interplate earthquakes, 3.31 MPa, given by Allmann and Shearer (2009). No evidence was observed regarding the dependence of stress drop on either magnitude or focal depth.

form of $Q_0 f^n$. The regression became $130.87f^{1.07}$ at frequencies ranging from 0.5 to 20.0 Hz, and its correlation coefficient was high. We should bear in mind that the obtained quality factors and their frequency dependence largely depend on the geometrical spreading function adopted in the spectral inversions. Based on separate analysis of the recordings obtained at stations in the Wellington and Christchurch regions, the resultant values of Q_0 and n were both found comparable at each distance bin, implying no significant regional dependence of anelastic attenuation in our study region.

Data and Resources

Strong-motion recordings used in this article were provided by the GeoNet Strong Motion Data Products at https://www.geonet.org.nz/data/types/strong_motion (last accessed September 2017). T_{site} and V_{S30} used in this study were collected from the New Zealand Strong Motion database of site metadata compiled by Kaiser, Houtte, *et al.* (2017) and available on the GeoNet website: <https://www.geonet.org.nz/data/supplementary/nzsmdb> (last accessed September 2017). The surface projection of the second segmentation of the fault rupture plane provided by the U.S. Geological Survey is available at <https://earthquake.usgs.gov/earthquakes/eventpage/us1000778i#finite-fault> (last accessed September 2017). Some of the plots were produced using Generic Mapping Tools (Wessel and Smith, 1991).

Acknowledgments

This work is supported by Science Foundation of Institute of Engineering Mechanics, China Earthquake Administration under Grant Number 2016A01 and National Natural Science Fund Numbers 51778589 and U1534202. The Guest Editor Anna Kaiser provided us with much background knowledge on the site characteristics in New Zealand, which made the discussions and conclusions of this study more fruitful. The authors thank Adrien Oth and one anonymous reviewer for their valuable suggestions and constructive comments, which helped us to improve the article.

References

- Aki, K. (1967). Scaling law of seismic spectrum, *J. Geophys. Res.* **72**, 1217–1231.
- Allmann, B. P., and P. M. Shearer (2009). Global variations of stress drop for moderate to large earthquakes, *J. Geophys. Res.* **114**, no. B01310, doi: [10.1029/2008JB005821](https://doi.org/10.1029/2008JB005821).
- Anderson, J. G., and S. Hough (1984). A model for the shape of the Fourier amplitude spectrum of acceleration at high frequencies, *Bull. Seismol. Soc. Am.* **74**, 1969–1993.
- Andrews, D. J. (1986). Objective determination of source parameters and similarity of earthquakes of different size, in *Earthquake Source Mechanics*, S. Das, J. Boatwright, and C. H. Scholz (Editors), AGU Monograph 37, 259–267.
- Atkinson, G. M., and D. M. Boore (1995). Ground-motion relations for eastern North America, *Bull. Seismol. Soc. Am.* **85**, 17–30.
- Atkinson, G. M., and R. F. Mereu (1992). The shape of ground motion attenuation curves in southeastern Canada, *Bull. Seismol. Soc. Am.* **82**, 2014–2031.
- Boore, D. M. (2003). Simulation of ground motion using the stochastic method, *Pure Appl. Geophys.* **160**, 635–676.
- Boore, D. M., and J. Boatwright (1984). Average body-wave radiation coefficients, *Bull. Seismol. Soc. Am.* **74**, 1615–1621.
- Bora, S. S., F. Scherbaum, N. Kuehn, P. Stafford, and B. Edwards (2015). Development of a response spectral ground-motion prediction equation (GMPE) for seismic-hazard analysis from empirical Fourier spectral and duration models, *Bull. Seismol. Soc. Am.* **105**, 2192–2218.
- Bradley, B. A. (2012). Ground motions observed in the Darfield and Christchurch earthquakes and the importance of local site response effects, *New Zeal. J. Geol. Geophys.* **55**, 279–286.
- Bradley, B. A. (2016). Strong ground motion characteristics observed in the 13 June 2011 M_w 6.0 Christchurch, New Zealand, earthquake, *Soil Dynam. Earthq. Eng.* **91**, 23–38.
- Bradley, B. A., and M. Cubrinovski (2011). Near-source strong ground motions observed in the 22 February 2011 Christchurch earthquake, *Seismol. Res. Lett.* **82**, 853–865.
- Bradley, B. A., H. N. T. Razafindrakoto, and V. Polak (2017). Ground-motion observations from the 14 November 2016 M_w 7.8 Kaikōura, New Zealand, earthquake and insights from broadband simulations, *Seismol. Res. Lett.* **88**, 1–17.
- Bradley, B. A., L. M. Wotherspoon, and A. E. Kaiser (2017). Ground motion and site effect observations in the Wellington region from the 2016 M_w 7.8 Kaikōura, New Zealand, earthquake, *Bull. New Zeal. Soc. Earthq. Eng.* **50**, 94–105.
- Bradley, B. A., L. M. Wotherspoon, A. E. Kaiser, B. R. Cox, and S. Jeong (2018). Influence of site effects on observed ground motions in the Wellington region from the M_w 7.8 Kaikōura, New Zealand, earthquake, *Bull. Seismol. Soc. Am.* **108**, doi: [10.1785/0120170286](https://doi.org/10.1785/0120170286).
- Brown, L. J., and J. H. Weeber (1992). Geology of the Christchurch urban area, *Institute of Geological and Nuclear Sciences Map*, GNS Science, Lower Hutt, New Zealand.
- Brune, J. N. (1970). Tectonic stress and the spectra of seismic shear waves from earthquakes, *J. Geophys. Res.* **75**, 4997–5009.
- Castellaro, S., and P. Bormann (2007). Performance of different regression procedures on the magnitude conversion problem, *Bull. Seismol. Soc. Am.* **97**, 1167–1175.
- Cubrinovski, M., B. A. Bradley, L. Wotherspoon, R. Green, J. Bray, C. Wood, M. Pender, J. Allen, A. Bradshaw, G. Rix, *et al.* (2011). Geotechnical aspects of the 22 February 2011 Christchurch earthquake, *Bull. New Zeal. Soc. Earthq. Eng.* **44**, 205–226.
- Cubrinovski, M., J. D. Bray, C. Torre, M. J. Olsen, B. A. Bradley, G. Chiaro, E. Stocks, and L. Wotherspoon (2017). Liquefaction effects and associated damages observed at the Wellington Centreport from the 2016 Kaikōura earthquake, *Bull. New Zeal. Soc. Earthq. Eng.* **50**, 152–173.
- Dellow, D., C. Massey, S. Cox, G. Archibald, J. Begg, Z. Bruce, J. Carey, J. Davidson, F. D. Pasqua, P. Glassey, *et al.* (2017). Landslides caused by the M_w 7.8 Kaikōura earthquake and the immediate response, *Bull. New Zeal. Soc. Earthq. Eng.* **50**, 106–116.
- Drouet, S., F. Cotton, and P. Gueguen (2010). V_{S30} , κ , regional attenuation and M_w from accelerograms: Application to magnitude 3–5 French earthquakes, *Geophys. J. Int.* **182**, 880–898.
- Dutta, U., N. Biswas, A. Martirosyan, A. Papageorgious, and S. Kinoshita (2003). Estimation of earthquake source parameters and site response in Anchorage, Alaska from strong-motion network data using generalized inversion method, *Phys. Earth Planet. In.* **137**, 13–29.
- Eberhart-Phillips, D., and S. Bannister (2010). 3-D imaging of Marlborough, New Zealand, subducted plate and strike-slip fault systems, *Geophys. J. Int.* **182**, 73–96.
- Eberhart-Phillips, D., M. Reyners, S. Bannister, M. Chadwick, and S. Ellis (2010). Establishing a versatile 3-D seismic velocity model for New Zealand, *Seismol. Res. Lett.* **81**, 992–1000.
- Fry, B., R. Benites, and A. Kaiser (2011). The character of accelerations in the M_w 6.2 Christchurch earthquake, *Seismol. Res. Lett.* **82**, 846–852.
- Fry, B., D. Eberhart-Phillips, and F. Davey (2014). Mantle accommodation of lithospheric shortening as seen by combined surface wave and teleseismic imaging in the South Island, New Zealand, *Geophys. J. Int.* **199**, 499–513.

- Hamling, I. J., S. Hreinsdottir, K. Clark, J. Elliott, C. Liang, E. Fielding, N. Litchfield, P. Villamor, L. Wallace, T. J. Wright, *et al.* (2017). Complex multi-fault rupture during the 2016 M_w 7.8 Kaikōura earthquake, New Zealand, *Science* **356**, doi: [10.1126/science.aam7194](https://doi.org/10.1126/science.aam7194).
- Hanks, T. C. (1982). f_{max} , *Bull. Seismol. Soc. Am.* **72**, 1867–1879.
- Hanks, T. C., and H. Kanamori (1979). A moment magnitude scale, *J. Geophys. Res.* **84**, 2348–2350.
- Hassani, B., H. Zafarani, J. Farjoodi, and A. Ansari (2011). Estimation of site amplification, attenuation and source spectra of S -waves in the east-central Iran, *Soil Dynam. Earthq. Eng.* **31**, 1397–1413.
- Henry, R. S., D. Dizhur, K. J. Elwood, J. Hare, and D. Brunson (2017). Damage to concrete buildings with precast floors during the 2016 Kaikōura earthquake, *Bull. New Zeal. Soc. Earthq. Eng.* **50**, 174–186.
- Hughes, M. W., M. Nayerloo, X. Bellagamba, J. Morris, P. Brabhaharan, S. Rooney, E. Hobbs, K. Wooley, and S. Hutchison (2017). Impacts the 14th November 2016 Kaikōura earthquake on three waters systems in Wellington, Marlborough and Kaikōura, New Zealand: Preliminary observations, *Bull. New Zeal. Soc. Earthq. Eng.* **50**, 306–317.
- Husid, P. (1967). *Gravity Effects on the Earthquake Response of Yielding Structures. Report of Earthquake Engineering Research Laboratory, California Institute of Technology, Pasadena, California.*
- Iizuka, H., Y. Sakai, and K. Koketsu (2011). Strong ground motions and damage conditions associated with seismic stations in the February 2011 Christchurch, New Zealand, earthquake, *Seismol. Res. Lett.* **82**, 875–881.
- Kaiser, A. E., N. Balfour, B. Fry, C. Holden, N. Litchfield, M. Gerstenberger, E. D'Anastasio, N. Horspool, G. McVerry, J. Ristau, *et al.* (2017). The 2016 Kaikōura, New Zealand, earthquake: Preliminary seismological report, *Seismol. Res. Lett.* **88**, 727–739.
- Kaiser, A. E., C. Holden, J. Beavan, D. Beetham, R. Benites, A. Celentano, D. Collett, J. Cousins, M. Cubrinovski, G. Dellow, *et al.* (2012). The M_w 6.2 Christchurch earthquake of February 2011: Preliminary report, *New Zeal. J. Geol. Geophys.* **55**, 67–90.
- Kaiser, A. E., C. V. Houtte, N. D. Perrin, L. Wotherspoon, and G. H. M. Verry (2017). Site characterisation of GeoNet stations for the New Zealand Strong Motion Database, *Bull. New Zeal. Soc. Earthq. Eng.* **50**, 39–49.
- Kaiser, A. E., A. Oth, and R. A. Benites (2013). Separating source, path and site influences on ground motion during the Canterbury earthquake sequence, using spectral inversions, *New Zealand Society for Earthquake Engineering Technical Conference*, Wellington, New Zealand, 26–28 April.
- Kaiser, A. E., A. Oth, C. Holden, R. Benites, and J. Haines (2016). Site amplification in Christchurch during the 2011–2011 Canterbury earthquake sequence, based on regional Fourier amplitude spectra (FAS) model, *5th IASPEI/IAEE International Symposium: Effects of Surface Geology on Seismic Motion*, Taipei, Taiwan, 15–17 August 2016.
- Kam, W. Y., S. Pampanin, and K. Elwood (2011). Seismic performance of reinforced concrete buildings in the 22 February Christchurch (Lyttelton) earthquake, *Bull. New Zeal. Soc. Earthq. Eng.* **44**, 223–233.
- Kanamori, H. (1994). Mechanics of earthquakes, *Annu. Rev. Earth Planet. Sci.* **22**, 207–237.
- Kanamori, H., and L. Rivera (2004). Static and dynamic scaling relations for earthquakes and their implications for rupture speed and stress drop, *Bull. Seismol. Soc. Am.* **94**, 314–319.
- Konno, K., and T. Ohmachi (1998). Ground-motion characteristics estimated from ratio between horizontal and vertical components of microtremor, *Bull. Seismol. Soc. Am.* **88**, 228–241.
- Laske, G., G. Masters, Z. Ma, and M. Pasyanos (2013). Update on CRUST1.0: A 1-degree global model of Earth's crust, *Geophys. Res. Abstr.* **15**, Abstract EGU 2013–2658.
- Litchfield, N. J., A. Benson, A. Bischoff, A. Hatem, A. Barrier, A. Nicol, A. Wandres, B. Lukovic, B. Hall, C. Gasston, *et al.* (2016). 14th November 2016 M_w 7.8 Kaikōura earthquake, *Preliminary Surface Fault Displacement Measurements*, Version 2, GNS Science, doi: [10.21420/G2J01F](https://doi.org/10.21420/G2J01F).
- Litchfield, N. J., R. Van Dissen, R. Sutherland, P. M. Barnes, S. C. Cox, R. Norris, R. J. Beavan, R. Langridge, P. Villamor, K. Berryman, *et al.* (2014). A model of active faulting in New Zealand, *J. Geol. Geophys.* **57**, 32–56.
- Mandal, P., and U. Dutta (2011). Estimation of earthquake source parameters in the Kachchh seismic zone, Gujarat, India, from strong-motion network data using a generalized inversion technique, *Bull. Seismol. Soc. Am.* **101**, 1719–1731.
- McCann, M. W. J., and H. C. Shah (1979). Determining strong motion duration of earthquakes, *Bull. Seismol. Soc. Am.* **69**, 1253–1265.
- Menke, W. (1989). *Geophysical Data Analysis: Discrete Inverse Theory*, in International Geophysics Series, Academic Press, New York, New York.
- Mortimer, N. (2004). New Zealand's geological foundations, *Gondwana Res.* **7**, 262–272.
- Mucciarelli, M. (2011). Ambient noise measurements following the 2011 Christchurch earthquake: Relationships with previous microzonation studies, liquefaction, and nonlinearity, *Seismol. Res. Lett.* **82**, 919–926.
- Nakano, K., S. Matsushima, and H. Kawase (2015). Statistical properties of strong ground motions from the generalized spectral inversion of data observed by K-Net, KIK-net, and the JMA Shindokei network in Japan, *Bull. Seismol. Soc. Am.* **105**, 2622–2680.
- Oth, A. (2013). On the characteristics of earthquake stress release variations in Japan, *Earth Planet. Sci. Lett.* **377/378**, 132–141.
- Oth, A., and A. E. Kaiser (2014). Stress release and source scaling of the 2010–2011 Canterbury, New Zealand earthquake sequence from spectral inversion of ground motion data, *Pure Appl. Geophys.* **171**, 2767–2782.
- Oth, A., D. Bindi, S. Parolai, and D. D. Giacomo (2010). Earthquake scaling characteristics and the scale-(in)dependence of seismic energy-to-moment ratio: Insights from KiK-net data in Japan, *Geophys. Res. Lett.* **37**, L19304, doi: [10.1029/2010GL044572](https://doi.org/10.1029/2010GL044572).
- Oth, A., D. Bindi, S. Parolai, and D. D. Giacomo (2011). Spectral analysis of K-NET and KiK-net data in Japan, part II: On attenuation characteristics, source spectra, and site response of borehole and surface stations, *Bull. Seismol. Soc. Am.* **101**, 667–687.
- Oth, A., D. Bindi, S. Parolai, and F. Wenzel (2008). S -wave attenuation characteristics beneath the Veranca region in Romania: New insights from the inversion of ground-motion spectra, *Bull. Seismol. Soc. Am.* **98**, 2482–2497.
- Oth, A., S. Parolai, D. Bindi, and F. Wenzel (2009). Source spectra and site response from S waves of intermediate-depth Vrancea, Romania, earthquakes, *Bull. Seismol. Soc. Am.* **99**, 235–254.
- Pacor, F., D. Spallarossa, A. Oth, L. Luzi, R. Puglia, L. Cantore, A. Mercuri, M. D'Amico, and D. Bindi (2016). Spectral models for ground motion prediction in the L'Aquila region (central Italy): Evidence for stress drop dependence on magnitude and depth, *Geophys. J. Int.* **204**, 697–718.
- Palermo, A., R. Liu, A. Rais, B. McHaffie, K. Andisheh, S. Pampanin, R. Gentile, I. Nuzzo, M. Granerio, G. Loporcaro, *et al.* (2017). Performance of road bridges during the 14 November 2016 Kaikōura earthquake, *Bull. New Zeal. Soc. Earthq. Eng.* **50**, 253–270.
- Papageorgiou, A. S., and K. Aki (1983). A specific barrier model for the quantitative description of inhomogeneous faulting and the prediction of strong ground motion. Part II. Applications of the model, *Bull. Seismol. Soc. Am.* **73**, 953–978.
- Parolai, S., D. Bindi, and P. Augliera (2000). Application of the generalized inversion technique (GIT) to a microzonation study: Numerical simulations and comparison with different site-estimation techniques, *Bull. Seismol. Soc. Am.* **90**, 286–297.
- Petersen, T., K. Gledhill, M. Chadwick, N. H. Gale, and J. Ristau (2011). The New Zealand National Seismograph Network, *Seismol. Res. Lett.* **82**, 9–20.
- Ren, Y. F., R. Z. Wen, H. Yamanaka, and T. Kashima (2013). Site effects by generalized inversion technique using strong motion recordings of the 2008 Wenchuan earthquake, *Earthq. Eng. Eng. Vib.* **12**, 165–184.

- Ristau, J., D. Harte, and J. Salichon (2016). A revised local magnitude (M_L) scale for New Zealand earthquakes, *Bull. Seismol. Soc. Am.* **106**, 398–407.
- Semmens, S., N. D. Perrin, and G. D. Dellow (2010). It's our fault—Geological and geotechnical characterisation of the Wellington Central Business District, *GNS Science Consultancy Report 2010/176 June.2010*.
- Smyrou, E., P. Tasiopoulou, I. E. Bal, and G. Gatetas (2011). Ground motions versus geotechnical and structural damage in the February 2011 Christchurch earthquake, *Seismol. Res. Lett.* **82**, 882–892.
- Stringer, M. E., S. Bastin, C. R. McGann, C. Cappellaro, M. El Kortbawi, R. McMahon, L. M. Wotherspoon, R. A. Green, J. Aricheta, R. Davis, et al. (2017). Geotechnical aspects of the 2016 Kaikōura earthquake on the South Island of New Zealand, *Bull. New Zeal. Soc. Earthq. Eng.* **50**, 117–141.
- Stirling, M. W., N. J. Litchfield, P. Villamor, R. J. V. Dissen, A. Nicol, J. Pettinga, P. Barnes, R. M. Langridge, T. Lettle, D. J. A. Barrell, et al. (2017). The M_w 7.8 2016 Kaikōura earthquake: Surface fault rupture and seismic hazard context, *Bull. New Zeal. Soc. Earthq. Eng.* **50**, 73–84.
- Tsuda, K., K. Koketsu, Y. Hisada, and T. Hayakawa (2010). Inversion analysis of site responses in the Kanto Basin using data from a dense strong motion seismograph array, *Bull. Seismol. Soc. Am.* **100**, 1276–1287.
- Tusa, G., A. Brancato, S. Gresta, and S. D. Malone (2006). Source parameters of microearthquakes at Mount St Helens (USA), *Geophys. J. Int.* **166**, 1193–1223.
- Wang, H. W., Y. F. Ren, and R. Z. Wen (2018). Source parameters, path attenuation, and site effects from strong-motion recordings of the Wenchuan aftershocks (2008–2013) using nonparametric generalized inversion technique, *Geophys. J. Int.* **212**, 872–890.
- Wessel, P., and W. H. F. Smith (1991). Free software helps map and display data, *Eos Trans. AGU* **72**, 441.
- Wotherspoon, L. M., R. P. Orense, B. A. Bradley, B. R. Cox, C. M. Wood, and R. A. Green (2015). Soil profile characterization of Christchurch Central Business District strong motion station, *Bull. New Zeal. Soc. Earthq. Eng.* **48**, 147–157.
- Wotherspoon, L. M., R. P. Orense, R. A. Green, B. A. Bradley, B. R. Cox, and C. M. Wood (2015). Assessment of liquefaction evaluation procedure and severity index frameworks at Christchurch strong motion stations, *Soil. Dynam. Earthq. Eng.* **79**, 335–346.
- Zhao, C. P., Z. L. Chen, W. Hua, Q. C. Wang, Z. X. Li, and S. H. Zheng (2011). Study on source parameters of small to moderate earthquakes in the main seismic active regions, China mainland, *Chin. J. Geophys.* **54**, 1478–1489 (in Chinese).

Key Laboratory of Earthquake Engineering and Engineering Vibration of
China Earthquake Administration
Institute of Engineering Mechanics, China Earthquake Administration
No. 29 Xuefu Road
Harbin, 150080
China
renyefei@iem.net.cn
joey052zy@163.com
whw1990413@163.com
ruizhi@iem.ac.cn

Manuscript received 30 September 2017;
Published Online 5 June 2018